PHYSICAL REVIEW E VOLUME 50, NUMBER 3 SEPTEMBER 1994

# Chaotic scattering in the presence of an external magnetic field

Wolfgang Breymann
*Institut für Physik, Universität Basel, Klingelbergstrasse 82, CH-4056 Basel, Switzerland*

Zoltán Kovács and Tamás Tél
*Institute for Theoretical Physics, Eötvös University, Puskin u. 5-7, H-1088 Budapest, Hungary*

(Received 21 October 1993; revised manuscript received 25 February 1994)

We study the chaotic scattering of charged particles in an open three-disk billiard subject to a uniform magnetic field. We identify qualitatively distinct behaviors depending on the field strength: hyperbolic, pruned, Kol'mogorov-Arnol'd-Moser torus dominated, and regular phases. The hierarchical structure of the chaotic set and the time delay function is investigated. Our main finding is that with increasing field strength the degree of chaoticity decreases while the complexity of the small scale structures may increase. Possible consequences of our results for the ballistic transport in microjunctions are discussed.

PACS number(s): 05.45.+b, 05.60.+w, 72.10.−d, 72.90.+y

## I. INTRODUCTION

In recent years, chaotic scattering has become a subject of intensive research because of both a strong theoretical interest and a wide range of potential applications [1–12]. The time a trajectory spends in the scattering region depends in such cases sensitively on the initial condition (e.g., on the impact parameter). The delay time distribution as a function of the impact parameter possesses singularities on a fractal set of dimension $D_0 \leq 1$ [7,8,2]. It is now understood that chaotic scattering is due to the existence of a *nonattracting chaotic set* [2] in phase space, which may be viewed as the closure of all unstable periodic orbits in the scattering region. The time delay function takes on an infinite value whenever the initial condition is placed on the stable manifold of any localized orbit. Since these orbits are organized in a fractal structure on the chaotic set, the infinities in the time delay function appear in the same fractal pattern. A study of the time delay function [9,12] provides thus the possibility to obtain important quantities characterizing the chaotic set, in particular its dimension, entropy, Lyapunov exponent, and escape rate. The singularities of the time delay function serve as a fingerprint of the chaotic set on the impact parameter axis. Because of the Hamiltonian character, in two-degree-of-freedom scattering processes the dimension of the chaotic set on a Poincaré plane is just $2D_0$.

So far, previous studies have concentrated mainly on scattering processes without any external field. The aim of this paper is to investigate how the presence of an external field influences the classical properties of chaotic scattering. We imagine that charged particles moving in a given scattering potential containing several potential hills become subject to a uniform magnetic field applied in the scattering region. This leads to the *breakdown of time reversal symmetry* (by simultaneously preserving the Hamiltonian character of the motion) and, consequently, to the appearance of a *preferred sign of curvature* in the trajectories. The form of the scattering function and the structure of the chaotic set depend on the field. The presence of the field also modifies the position and stability of periodic orbits. Moreover, a sufficiently strong field can stabilize periodic orbits which are unstable in the field-free case. Such orbits become nonaccessible for scattering trajectories. It is also clear that strong fields can make the motion regular by forcing particles to wind around one potential hill only. Because of the localization, they cannot interact with other parts of the potential. Thus the external field can be used *to make the scattering process nonchaotic.*

We are interested in the situation where in the field-free case the chaotic scattering at a given particle energy is *hyperbolic* [2]. This means that all periodic orbits possess strictly positive Lyapunov exponents and the symbol sequences associated with them form a *complete* symbolic encoding of the chaotic set. Hyperbolicity implies that there are no Kol'mogorov-Arnol'd-Moser (KAM) surfaces in the phase space. We shall point out that the following scenario is observed by switching on a magnetic field. A weak field can only deform the chaotic set, but does not destroy hyperbolicity because of its structural stability. However, even a weak field makes the process quantitatively *less* chaotic. This is expressed by the change of characteristic quantities: the average Lyapunov exponent $\overline{\lambda}$ on the chaotic set decreases, the average chaotic lifetime $\tau$ and the fractal dimension of singularities $D_0$ increase, while the topological entropy $K_0$ stays unchanged. At intermediate field strengths hyperbolicity breaks down and *pruning* [13] sets in, i.e., more and more periodic orbits become forbidden. For systems with smooth potentials this is accompanied by the appearance of stable periodic orbits and KAM surfaces around them, but the latter are hardly visible at first. Nonhyperbolicity is first reflected in a *decrease* of the topological entropy $K_0$ marking a further reduction of chaoticity. By increasing the field strength further, the KAM surfaces become dominating: many trajectories will stick to them so that the average Lyapunov exponent $\bar{\lambda}$ tends toward zero. The average lifetime $\tau$ is defined as the reciprocal value of the decay rate (sometimes called *escape rate*) of the exponential lifetime distribution. Since the probability of finding a given lifetime is characterized by a power law in the presence of tori [14,12], the escape rate is formally zero in such cases; the lifetime may be infinite or finite depending on the exponent in the power law. Simultaneously, the fractal dimension $D_0$ is expected to tend to unity [12]. Thus *hyperbolic chaos disappears in the asymptotic behavior on the chaotic set,* although on finite time scales it may be observed numerically. This is also supported by the fact that the topological entropy is still nonzero, i.e., there is an infinity of periodic orbits in the system, many of them being definitely hyperbolic. Finally, at strong fields, periodic orbits gradually disappear and the topological entropy tends to zero. In the course of this process, chaos becomes less and less important in the sense that the supporting interval of the irregular part of the time delay function gradually shrinks to zero.

As a model for studying this scenario in detail, it is worth investigating the limit of infinitely steep potential hills corresponding to an *open billiard* system. In particular, we choose the three-disk problem, the field-free version of which has been extensively studied [15,16]. The presence of hard walls makes the analytic derivation of a Poincaré map possible, even in nonzero magnetic field, and the numerical work becomes much easier than in systems with smooth hills. The semiclassical treatment of the three-disk problem in a magnetic field has been worked out very recently [17], concentrating mainly on parameter settings where the classical problem is hyperbolic. Our main aim here is to follow the field dependence of the scattering process in the classical case which is dominated by nonhyperbolic effects.

The paper is organized as follows. The model and its most important features are described in Sec. II, while the derivation of the explicit form of the Poincaré map is relegated to Appendix A. Next, we study how the structure of the chaotic set changes with the magnetic field $B$ and compare it to the behavior of the corresponding time delay function (Sec. III). By looking at the detailed structure of the time delay distribution, different length scales can be defined in some hierarchical organization. The ones covering the singularities can best be used for evaluating quantitative characteristics of the scattering process by applying the method of the thermodynamic formalism of dynamical systems. The results as a function of $B$ are given in Sec. IV. Our conclusions are presented in Sec. V, where we also discuss the implications of our results for a branch of mesoscopic phenomena: ballistic transport in semiconductor microstructures.

## II. MODEL

The scattering potential of the system is provided by the hard walls of three identical disks of radii $r$ placed on the corners of a regular triangle of edge size $2d$. The ratio $d/r$ is fixed to $2/\sqrt{3}$ throughout this paper. The midpoint of the triangle coincides with the origin of the $(x, y)$ plane, and our frame of reference is chosen as shown in Fig. 1. We consider the motion of charged particles subject to a uniform magnetic field perpendicular to the $(x, y)$ plane and restricted to a region around the disks to be specified below. Particles of unit mass are injected into the system with a given velocity which means fixing the particle energy. Outside the region where the field is nonzero, trajectories are straight line segments. As soon as the particles enter the support of the field, they start to move on circular orbits because of the Lorentz force with an unchanged magnitude of the velocity. We choose the units in such a way that the radius of all circular orbits, the cyclotron radius, is

$$s \equiv \frac{1}{B}, \tag{1}$$

where $B$ stands for the magnetic field strength. The signs of charge and field are fixed so that the motion of the particles along the arcs is counterclockwise.

Specular collisions with the walls induce jumps from one circular orbit onto another one of the *same* cyclotron radius $s$. Thus the whole scattering process inside the interaction region can be kept track of by following the positions of the centers of these circles. A jump in the center position always occurs when the particle collides with a disk. Thus the sequence of the circle centers provides a discrete map (a Poincaré map) associated with the time continuous dynamics. Let $P(p, q)$ denote the orbit center at a given instant of time. After collision, a new center $P'(p', q')$ defines the particle trajectory. The Poincaré map $T$ connecting these coordinates relative to the position of the disk on which the collision occurs,

$$(p', q') = T(p, q), \tag{2}$$

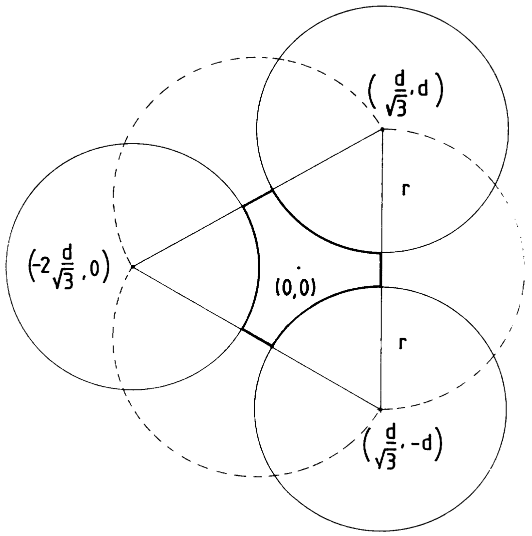

FIG. 1. Geometry of the three-disk problem for $d = \sqrt{3}, r = 1.5$, a case we shall investigate throughout the paper. The boundary of the support of the field is denoted by dashed lines. Heavy lines define the central region outside of which a particle immediately escapes.

can be explicitly computed and is given in Appendix A (see also Fig. 2). The complete dynamics can then be described by subsequent applications of this map with the proper disk center coordinates. $p$ and $q$ are canonically conjugate pairs and the plane $(p, q)$ is taken as the phase space of this process.

Just like in many other examples of nonlinear systems, the knowledge of the symbolic dynamics is of essential help in characterizing chaotic scattering. In the field-free case of the three-disk problem, bouncing twice on the same disk without hitting another one in between is impossible. Thus two symbols are sufficient for encoding. With the exception of geometrical arrangements with large disk radii the scattering is hyperbolic and all possible binary sequences are realized by the symbol sequences of unstable periodic orbits. One may, for example, use the code 0 for collisions turning the particle back toward the disk where it started and the symbol 1 if it is reflected toward another disk. This encoding makes use of the $C_{3v}$ symmetry of the system and does not distinguish between trajectories that are transformed into each other by a rotation of $2\pi/3$ around the origin or a reflection on a symmetry axis of the triangle. In the presence of a magnetic field, however, this symmetry is reduced to the simple $C_3$ rotational symmetry, which means one has to use another encoding. We associate therefore codes with circular orbit segments between two subsequent collisions (rather than with the collisions themselves) so that 0 (1) corresponds to an orbit segment connecting two disks in a clockwise (counterclockwise) sense. At strong fields the introduction of a third symbol may also be necessary to describe two or more subsequent collisions on the same disk. It is worth noting that time reversal and reflection are individual symmetries only in the field-free case, but the combined symmetry survives the application of the magnetic field and becomes a nontrivial symmetry of the system.

The basic periodic orbits, just like in the field-free case, correspond to the bouncing motion between two neighboring disks and to the permanent rotation between the disks (see Fig. 3). The latter can be clockwise or counterclockwise representing two different period-1 orbits encoded by $\overline{0}$ and $\overline{1}$, respectively, in the symbolic dynamics described above. The bouncing between neighboring disks is the only primitive period-2 orbit $\overline{01}$. It provides an example of an orbit which is invariant, even in the presence of a field, under the *combined* symmetry of time reversal and reflection.

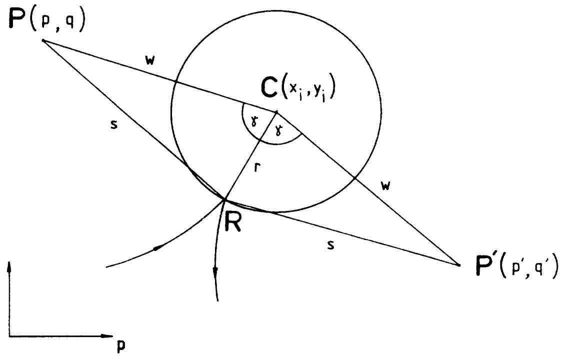

FIG. 2. Diagram for the determination of the Poincaré map $(p', q') = T(p, q)$ (for details, cf. Appendix A).

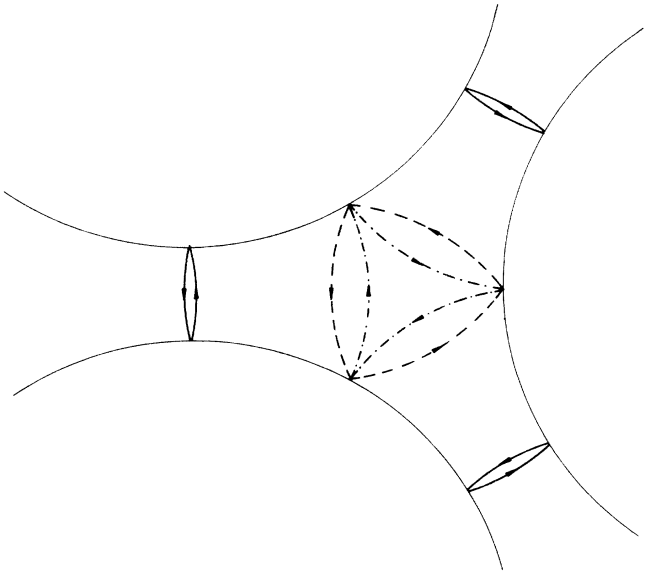

FIG. 3. Basic periodic orbits. Full lines, bouncing orbits $\overline{01}$ between neighboring disks, dashed and dash-dotted lines, time-reversed ring orbits $\overline{1}$ and $\overline{0}$, respectively.

The period-2 orbit $\overline{01}$ is the bounded orbit which lies furthest away from the origin. It is convenient to choose the support of the magnetic field such that it contains all three period-2 orbits $\overline{01}$ connected by the rotational symmetry. Simultaneously, it is advantageous to avoid the possibility of a complete winding around a given disk. As a choice independent of the field strength, we take for the support of the field the regular triangle defined by the disk centers augmented by three semicircles of radii $d$ sitting on the edges (of length $2d$) of the triangle. Note that there also exists a central region (marked by heavy lines in Fig. 1) with the property that any collision outside of it results in an unbounded (escaping) trajectory.

By means of the map (2), one can explicitly compute the Lyapunov exponents of the basic periodic orbits. We find that the fixed points $\overline{0}$ and $\overline{1}$ have different field-dependent Lyapunov exponents, but the period-2 orbit $\overline{01}$ possesses the same exponent as in the field-free case (cf. Appendix A). These effects, used in a simple approximation, are sufficient to predict the kind of changes induced in the scattering characteristics at low field strength at least (see Appendix B).

## III. THE CHAOTIC SET AND THE TIME DELAY FUNCTION

The hallmark of chaotic scattering in experimental data is the presence of singularities arranged in a fractal structure in the scattering functions [7,2]. To obtain, e.g., the time delay function, one takes a one-parameter family of initial conditions for scattering (a line or a simple curve in configuration space or phase space) and measures the time needed for the particle to leave the scattering region as a function of the parameter. (Note that here and in the following, time is measured in the *number of bounces*.) The irregular behavior of this function is caused by the existence of a chaotic set in phase space that contains all the bounded orbits of the system. Although the structure of the singularities in the time delay function reflects the structural properties of the chaotic set, the fact that we choose a one-dimensional set of initial conditions may cause this information to appear in a distorted form in the time delay data. For this reason, it is also worth visualizing the chaotic set in the Poincaré section to learn how it evolves as we vary the magnetic field and comparing these changes to the observed behavior of the time delay function.

For the three-disk model introduced in Sec. II, the chaotic set can be displayed using the center coordinates $(p,q)$ of circular segments taken from a long trajectory staying in its close vicinity. To achieve this, we used the so-called proper interior maximum triple method of Nusse and Yorke [18] that yields a long sequence of very small segments (called a *saddle-straddle orbit*) assumed to straddle a true orbit on the chaotic set. In Figs. 4–6 we plotted the approximation of the chaotic set obtained in this way for a few values of the cyclotron radius $s$. Due to the threefold symmetry of the system, the set consists, in all cases, of three identical pairs of blocks arranged along a circle of radius $s$ centered at the origin. Within the pairs, the blocks differ both in shape and size as a consequence of the lack of reflectional and time reversal

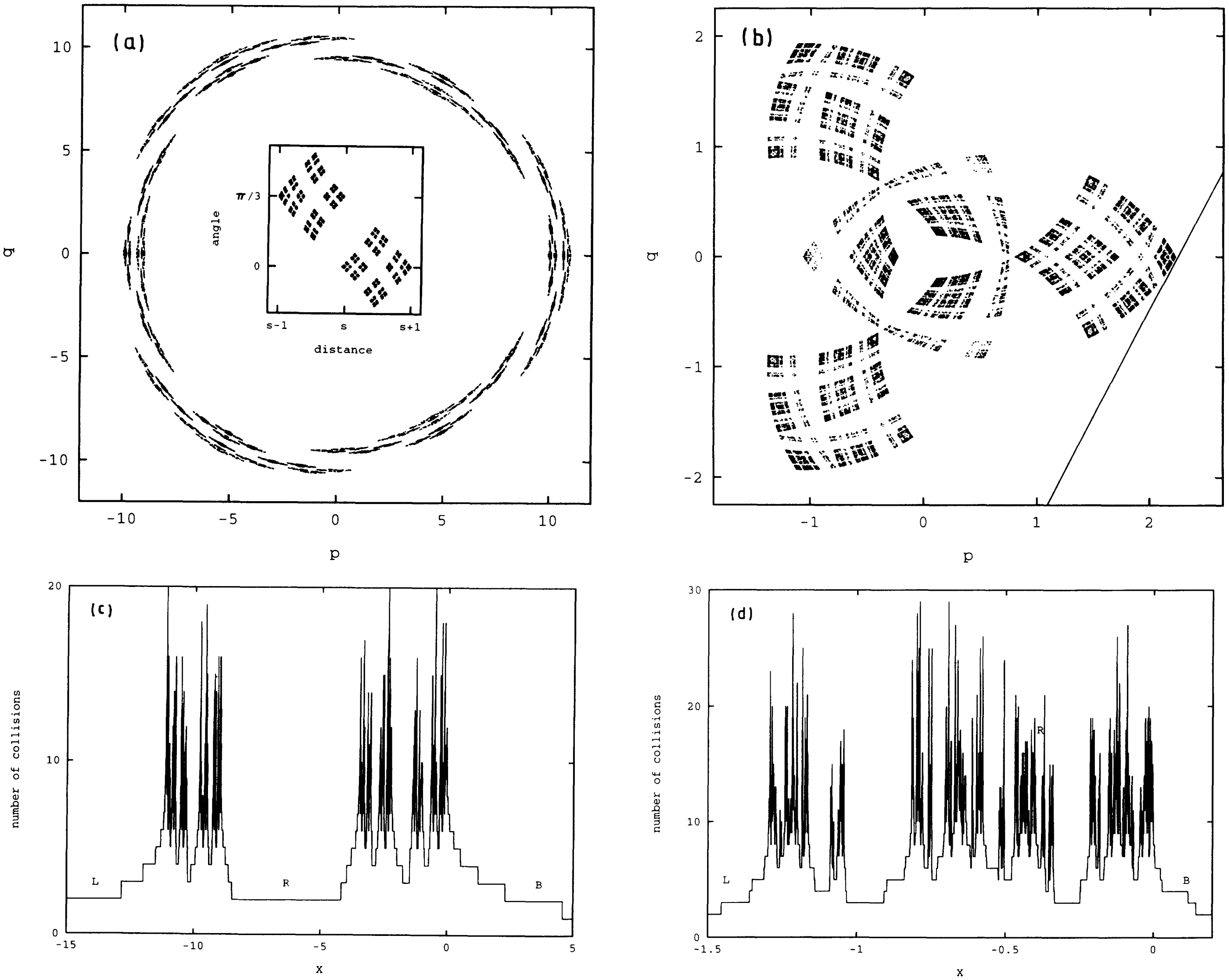

FIG. 4. The chaotic set and the time delay function of the three-disk system for values of the cyclotron radius $s$ when the chaotic set is hyperbolic. (a) The chaotic set for $s = 10$; the inset shows the structure of the rightmost and upper right blocks obtained by an affine transformation. (b) The chaotic set for $s = 1.25$. The straight line, which is parallel to the unstable manifold of the $\overline{01}$ orbit, illustrates the type of initial conditions taken for the time delay functions in this figure and throughout the paper. (c) and (d) display the time delay functions corresponding to (a) and (b), respectively. $X$ is the coordinate along the line of initial conditions measured from the crossing with the $p$ axis ($X > 0$ for $q > 0$). The narrow hole marked by $R$ in (d) corresponds to the first-level large central hole of (c) (see text).

symmetry; this difference, however, tends to diminish for weak fields, i.e., $s \gg r$ [see the inset of Fig. 4(a)]. Note the axial symmetry of both the individual blocks and the whole set: it is a consequence of the combined time reversal–reflection symmetry mentioned in Sec. II.

To construct the time delay function, we take as initial conditions (i.e., centers of the first circular parts of the trajectories) a straight line segment in the $(p, q)$ plane that starts close to one point of the $\overline{01}$ cycle (a "corner" point of the chaotic set) in the direction of its unstable manifold [cf. the line drawn in Fig. 4(c)]. This segment, which lies completely outside the chaotic set, corresponds to trajectories starting from the line segment in configuration space that connects the centers of the upper and the lower disks with suitable directed velocities. For not too weak fields, the line of initial conditions in phase space crosses the stable manifold of the chaotic set. Thus this line segment is suitable to obtain the time delay function for our model. (In the weak-field limit a circular arc is more suitable for this purpose to follow the curvature of the side of the chaotic set.) In addition to the plots of the chaotic sets, Figs. 4–6 show the corresponding time delay functions. The values of the cyclotron radius are the same as the ones taken for the plots of the chaotic set.

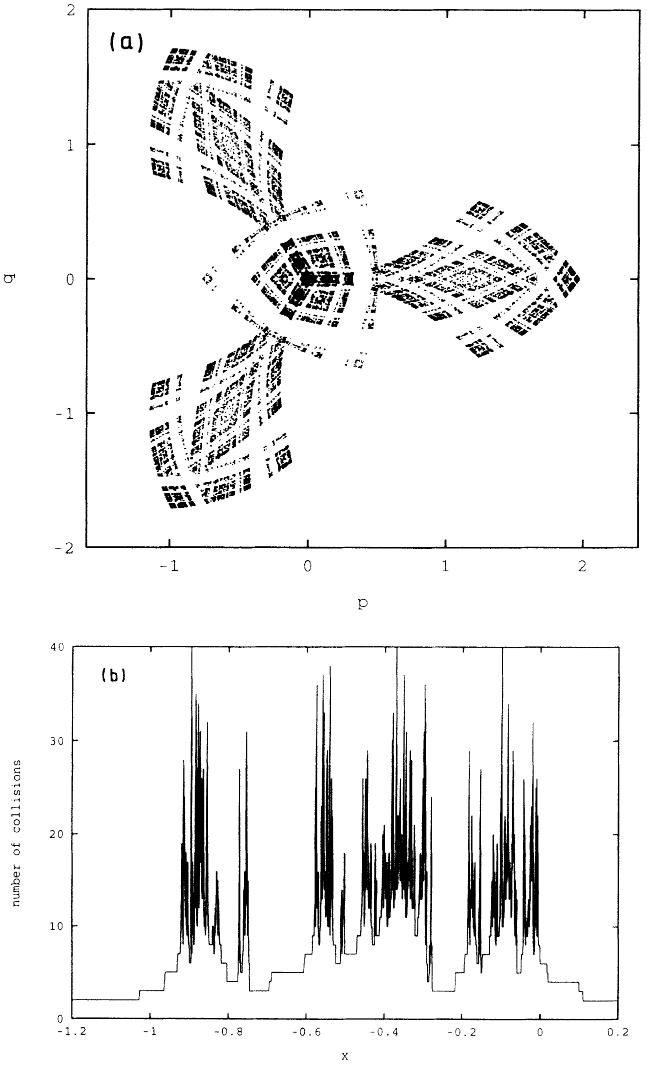

FIG. 5. (a) The chaotic set for $s = 1.0$ when pruning has set in. Some corners of the blocks have collided and disappeared. (b) The corresponding time delay function. The first level hole $R$ of Fig. 4(d) is missing here.

Figure 4 exhibits two cases where the chaotic set is hyperbolic with a complete binary encoding. The binary organization of the set, which is obviously locally equivalent to the direct product of two Cantor sets, is reflected in the structure of the time delay function as well: A cross section of the time delay function that contains all points where the time delay is not shorter than 3 consists of two large parts. Each of them disintegrates into two smaller parts when we take the cross section at the next higher value of the time delay, and these again disintegrate into smaller and smaller parts and so on for higher and higher time delays, giving rise to a self-similar structure with hierarchical organization (Fig. 7). The "holes" separating these blocks can be characterized by common properties of trajectories starting out of them. In particular, all trajectories with initial condition inside a given hole leave the scattering region through the same exit after the same number of iterations. That means the holes, together with the smooth sections at the two sides of the plot, can be labeled according to the possible exits: $B$ for backscattering (i.e., exit into the "channel" used for entering) and $L$ and $R$ for the left and right exit channels, respectively (see Fig. 7).

The level at which a hole appears is determined by the number of collisions of its trajectories; e.g., the principal hole $R$ at the first level contains trajectories with the smallest possible number of collisions allowed by the geometry of the system. On the specified line segment of initial conditions, the overall length of all the holes with the same label, independent of their level in the hierarchy, is proportional to the transition probability from the entrance (which is the same on the whole line segment) to the exit with that label. Therefore, it provides us with an important and experimentally accessible piece of information. Since the lengths of the holes shrink exponentially as we go higher in the hierarchy, it is sufficient to identify and to measure the holes of the first few levels.

By increasing the magnetic field, i.e., decreasing the cyclotron radius $s$, one reaches a critical value $s_1 \approx 1.24$ at which pruning sets in. The specific value of $s_1$ follows from the geometric condition that some orbits become tangential to a disk. Figure 5(a) shows the chaotic set for a case with $s < s_1$. In this plot, an important detail to pay attention to is that pieces of the chaotic set have collided in some regions, causing some orbits to disappear. In the corresponding time delay plot [Fig. 5(b)] this phenomenon is marked by the disappearance of some exits in different regions. The first-level exit labeled $R$ is, for example, large in Fig. 4(c), becomes very narrow in Fig. 4(d), and has completely disappeared in Fig. 5(b). One should also note that in these figures there is no sign of the existence of stable orbits, which means that all the allowed orbits in the system are still unstable.

If we reduce the cyclotron radius further, we enter the

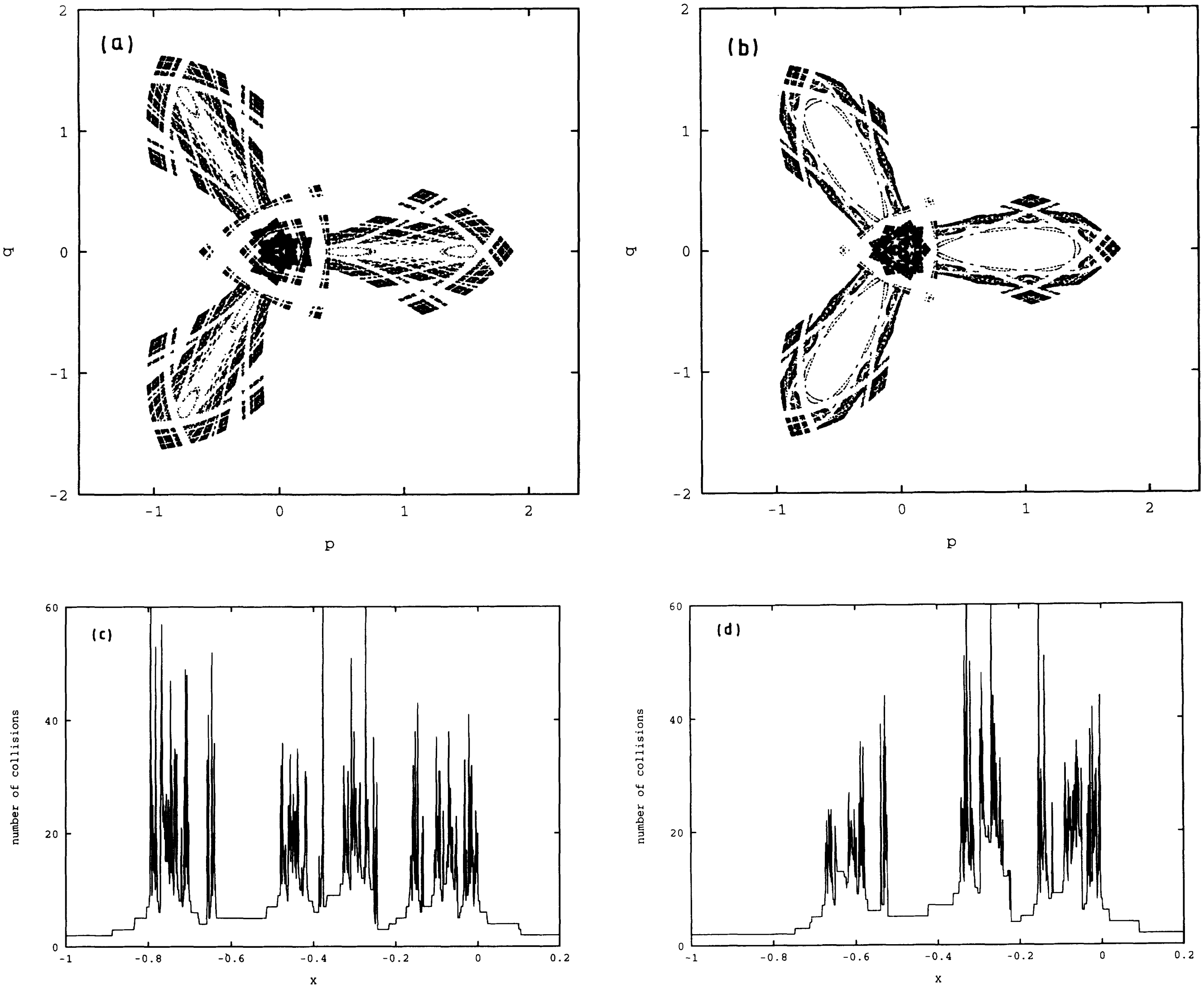

FIG. 6. The chaotic set for $s = 0.9$ (a) and 0.8 (b) with stable islands and the corresponding time delay plots [(c) and (d), respectively].

region $s < s_2 \approx 0.92$ where some orbits become stable (Fig. 6). These orbits sit in the middle of stable islands surrounded by KAM tori (smooth curves of quasiperiodic motion), which can easily be identified in the phase space plot of the chaotic set as empty elliptical holes. It has to be emphasized that the elliptic orbits and the inside of the stable islands, around them are not accessible for scattering trajectories. The boundary of the islands is, however, visible because trajectories getting close to a KAM torus can stay for an anomalously long time in its neighborhood. This phenomenon is marked in the time delay plot by the presence of dense, broadened parts with high time delay values in the neighborhood of initial conditions that lead to trajectories approaching a KAM torus. Comparing these plots to those of the chaotic set, however, we see that the signs of the existence of stable islands are less easy to discern in the time delay function

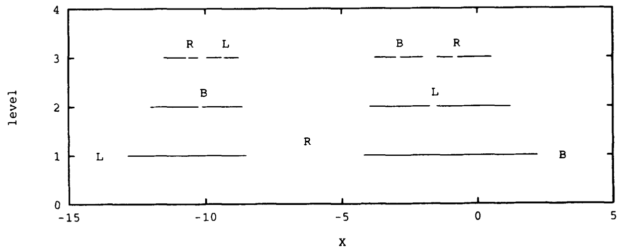

FIG. 7. The first few levels of the hierarchical organization of the time delay function for $s = 10$ [see Fig. 4(c)]. The intervals at level $n$ correspond in this case to initial conditions allowing at least $n + 3$ collisions with the disks. The holes between the intervals are marked according to the exit their trajectories take when leaving the system. The lengths of these intervals are the input data to the thermodynamical analysis of the scaling properties [see Eq. (3)].

because it is the *fine* structure of the function around a singularity that changes in this case.

An important effect of the magnetic field on scattering is that the size of the region characterized by singular behavior gradually shrinks for stronger field values. One can observe this effect in the time delay plots (compare, e.g., the scales and the portions of the singular parts in Figs. 4–6). This shrinking behavior is also present in the plots of the chaotic set: the area covered by the basic blocks decreases with $s$; in addition, in the cases with KAM tori, a part of that area is lost to the stable islands, leaving less room for chaotic scattering trajectories. This is to be contrasted with another consequence mentioned earlier, namely, the increase of the fractal dimension of the singularities and the chaotic set. Together they imply that strong fields reduce the overall weight of the chaotic features in scattering. On the other hand, the remaining chaotic regions show a denser and more complicated structure.

## IV. SCALING PROPERTIES

A quantity of central interest that reflects the hierarchical organization of chaotic scattering processes is the free energy $F(\beta)$. It characterizes the scaling behavior seen by following trajectories with an increasing number $n$ of collisions inside the scattering center [9]. The free energy is introduced in the spirit of the thermodynamic formalism of dynamical systems [19–21] via the relation

$$\sum_{i}^{N(n)} \left(l_i^{(n)}\right)^{\beta} \sim e^{-\beta F(\beta) n}, \tag{3}$$

where $\beta$ is an arbitrary real number and $n \gg 1$. The $l_i^{(n)}$ $[i = 1, \ldots, N(n)$, where $N(n)$ is the number of level-$n$ intervals] denote the lengths of intervals $I_i^{(n)}$ lying along a straight line chosen arbitrarily in the configurational space and having the following common property: trajectories starting out of these intervals with a given velocity vector have *at least* $n$ collisions with the disks before they leave the scattering region. In other words, $I_i^{(n)}$ are intervals where the delay function is greater than or equal to $n$ (see also Fig. 7). Equivalently, one can also use the length scales generated on a straight line in a Poincaré plane by considering trajectories which do not leave a certain neighborhood of the chaotic set earlier than at the $n$th step [9]. In any case, it is an essential part of the definition of the intervals at level $n$ that trajectories starting in the interior of a given interval should exhibit the same qualitative behavior up to $n$ steps: they possess the *same symbolic dynamics* over $n$ collisions. Obviously, both the interval lengths $l_i^{(n)}$ and the free energy $F(\beta)$ depend on the magnetic field.

In hyperbolic cases the criterion of having the same code inside an interval is automatically fulfilled since different symbol sequences of length $n$ always mark intervals well separated from each other in space by holes containing escaping trajectories with less than $n$ collisions. After pruning sets in, some exits might be forbidden (cf. Fig. 5) and therefore intervals of level $n$ characterized by different codes may come into contact. Consequently, the intervals cannot be separated with certainty by investigating the value of the time delay alone. The simultaneous use of the symbolic dynamics and the time delay is thus essential in computing the free energy in the range of the magnetic field where pruning is present, i.e., for $s < s_1$.

It is worth summarizing briefly some basic features of the free energy function [9]. The graph $\beta F(\beta)$ vs $\beta$ is monotonically increasing with a nonpositive second derivative. In the language of thermodynamics, this corresponds to the positivity of the specific heat. The value of $\beta F(\beta)$ taken at 1 and 0 immediately yields two basic characteristics of the scattering process: the escape rate and the topological entropy, respectively. The escape rate $\kappa$ describes the exponential decay of the total interval length $\sum_i l_i^{(n)}$ with $n$. Thus

$$\kappa = F(1). \tag{4}$$

As long as no KAM tori are present, $\kappa$ is nonzero and $1/\kappa$ yields the average chaotic lifetime $\tau$ of scattering trajectories. The topological entropy $K_0$ can be defined as the quantity characterizing the exponential growth of the number $N(n)$ of intervals $I_i^{(n)}$ with the level index $n$. Since the total number $N(n)$ of intervals is obtained from Eq. (3) at $\beta = 0$, we obtain

$$K_0 = -[\beta F(\beta)]\,|_{\beta=0}\ . \tag{5}$$

Note that $K_0$ also appears as the exponential growth rate of the number of *smooth* pieces in the time delay function.

If the chaotic set is hyperbolic, length scales and natural measures of the intervals are proportional. Therefore, the free energy also contains relevant information concerning metric properties. It is easy to show that it uniquely specifies the entire multifractal spectra of Lyapunov exponents [22] ($\lambda_q$), of entropies [23] ($K_q$), and of partial dimensions [24,25] ($D_q$) taken with respect to the natural measure of the chaotic set. Due to the Hamiltonian character of the system, the partial dimensions along the stable and unstable directions coincide. In nonhyperbolic cases when KAM surfaces are present, the relations between the free energy and different multifractal spectra still hold in a *restricted* range of the $\beta$ variable, typically for $\beta \leq 1$.

Here we shall concentrate on quantities which in our view are the most important characteristics of the scattering process. These are, in addition to the escape rate $\kappa$ and the topological entropy $K_0$, the average Lyapunov exponent $\overline{\lambda}$ and the fractal dimension $D_0$ of the singularities in the time delay function. They can be obtained as the derivative of $\beta F(\beta)$ taken at unity and as the value of $\beta$ where the free energy vanishes, respectively, i.e., as

$$\overline{\lambda} = [\beta F(\beta)]'\,|_{\beta=1}, \tag{6}$$

and

$$F(D_0) = 0. \tag{7}$$

In the presence of KAM surfaces, the delay time distribution decays more slowly than exponentially [14,12] and the long-time behavior is dominated by scattering trajectories exhibiting quasiperiodic motion for a long period of time. Consequently, both the escape rate and the average Lyapunov exponent should be zero in the asymptotic limit. On general grounds one expects [12] that the fractal dimension tends to unity. Since the decay of the length scales $l_i^{(n)}$ is no longer exponential in $n$ and the length scales are not neccessarily proportional to the natural measures, relations between the free energy and multifractal spectra break down. Formula (5) for the topological entropy is, however, still valid in this case.

Numerically, we have computed an approximate free energy $F^{(n)}(\beta)$ at level $n$ as

$$\beta F^{(n)}(\beta) = -\ln \frac{\sum\limits_{i}^{N(n)} \left(l_i^{(n)}\right)^{\beta}}{\sum\limits_{i}^{N(n-1)} \left(l_i^{(n-1)}\right)^{\beta}}, \tag{8}$$

which, because of Eq. (3), should tend to the exact free energy $F$ when $n \to \infty$. In a numerical computation, of course, this limit cannot be performed. Fortunately, in many cases the convergence is very fast and we obtain rather accurate results by computing the approximate free energy at some maximum value $n_{\max} \approx 15$. The error of the computation at a given $\beta$ can be estimated by analyzing the fluctuations of $F^{(n)}(\beta)$ in a range of $n$ below $n_{\max}$, say, in the interval $(n_{\max} - 5, n_{\max})$. With the exception of cases where KAM tori exist, the relative error turned out to be less than 1% in the entire range of $-5 < \beta < 5$.

The free energy obtained in this way is exhibited in Fig. 8 at various field strengths in cases where no KAM surfaces are present. As long as pruning does not appear (i.e., for cyclotron radii $s \geq s_1$), the topological entropy is independent of the magnetic field and takes the value $\ln 2$. The qualitatively new effect of pruning is the decrease of the topological entropy, which can be seen in the figure [cf. also Fig. 12(b) below]. It is worth emphasizing that the asymptotic slope for positive $\beta$ of $\beta F(\beta)$ *decreases* with increasing magnetic field. This implies that the longest intervals shrink more and more slowly or, equivalently, that the unstable periodic orbits with the smallest Lyapunov exponent on the chaotic set become less and less unstable.

Special attention has to be paid to cases where KAM surfaces of macroscopic size are present. Since the escape rate and the Lyapunov exponent are zero, while the fractal dimension is unity, the free energy must reach the horizontal axis at $\beta = 1$ with zero slope. From its monotonic increase with a never positive second derivative it follows that $\beta F(\beta)$ is identically zero for any value $\beta \geq 1$. Figure 9(a) shows the form one expects for the exact free energy function. It has been computed by taking initial points $(p, q)$ in the phase space along a horizontal line cutting through the KAM tori. Their existence implies the appearance of intervals the length of which converges very fast to the diameter of the torus and from then on does not change at all with $n$. This leads immediately to the expected behavior.

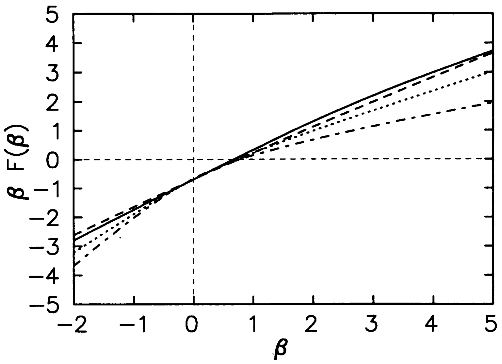

FIG. 8. Free energy obtained for cyclotron radii $s = 10.0$ (full line), 1.25 (dotted), and 1.0 (dash-dotted) with initial conditions of the type shown in Fig. 4(b). We plotted $F^{(14)}$ defined by Eq. (8), which deviates from $F^{(n)}$ with $n = 10, \ldots, 13$ by less than 1% in the $\beta$ range investigated. For comparison, the result of the four-scale approximation (see Appendix B) is also shown for $s = 10.0$ (dashed line). Note that the curvature of the graphs increases with decreasing $s$. From the decreasing slope of the asymptote for $\beta \to \infty$ it follows that the escape rate and the average Lyapunov exponent decrease and the fractal dimension increases. The topological entropy for $s = 10.0$ and 1.25 is $K_0 = \ln 2$, but for $s = 1.0$ it is definitely less.

The type of initial condition used here is obviously of no relevance for scattering processes since initial coordinates of particles are located in the region of asymptotically free motion and thus cannot lie inside any torus. We just chose it to illustrate what the exact free energy looks like and to compare it with the results obtained with more realistic initial conditions. The approximate free energy $F^{(n)}$ is plotted in Fig. 9(b) for levels between $n = 10$ and 14 obtained with initital coordinates corresponding to scattering conditions. The tendency toward zero is evident for $\beta > 1$, although the convergence is rather slow. This reflects the presence of intervals, the size of which decays algebraically with $n$. The slow and not necessarily monotonous convergence may be due to the fact that trajectories staying close to the KAM surface contain qualitatively different circular segments that contribute very differently to the finite-time Lyapunov exponent of the orbit. A similarly slow convergence has also been found at other values of the field strength.

It is instructive to look at the Legendre transform $S(E)$ of the free energy, which in the language of the thermodynamic formalism corresponds to an entropy function [9,10]. By plotting it for different values of the field strength (Fig. 10), one can notice that the support of $S(E)$ increases. This means that the spectrum of local Lyapunov exponents is broadening until it reaches the origin when KAM tori appear.

The fact that in a range of the inverse "temperature" $\beta$ the free energy becomes identically zero corresponds to the occurrence of a phase transition [26,27]. The slow convergence with $n$ can be interpreted as a consequence of enhanced fluctuations. This is fully supported by computing the fluctuations of the approximate free energy

$F^{(n)}$ by taking different values of $n$ at a fixed $\beta$ and plotting the results for different field strengths. Figure 11 exhibits the fluctuations of $F^{(n)}(1)$ corresponding to the same initial conditions as in Fig. 9(b). The fluctuations are negligible at first, but around the point $s_2 \approx 0.92$, where KAM tori appear, they start to grow. Below $s_2$ the variance becomes larger by orders of magnitudes. Thus we conclude that the free energy cannot be computed numerically in a reliable way for $\beta \geq 1$ if KAM tori are present in the system. For the values of escape rate, Lyapunov exponent, and fractal dimension the analytically known exact results have to be taken.

Finally, we summarize in Fig. 12 the field dependence of the most important characteristic quantities in the range investigated. The tendency found in the hyperbolic cases does not change: the dimension increases until it reaches unity and the escape rate and the Lypunov exponent decrease and become zero at the appearance of macroscopic KAM tori. It is worth emphasizing that this occurs at a cyclotron radius which is still much larger than the critical radius $s_c = d - r \approx 0.23$, where any sign of chaoticity disappears.

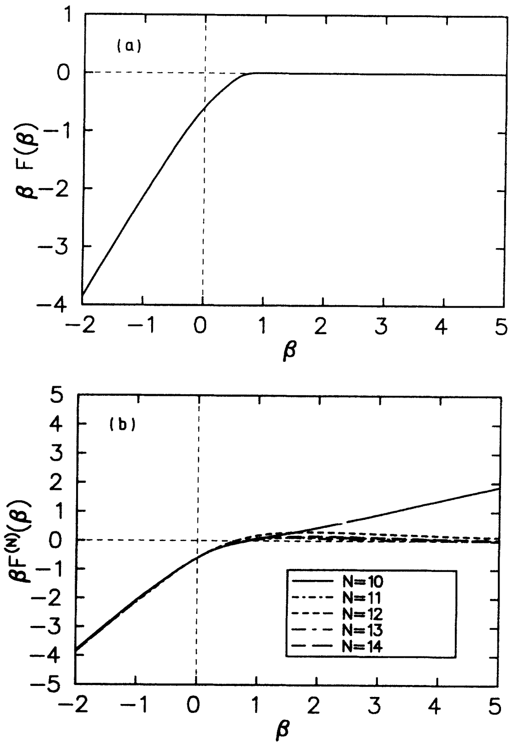

FIG. 9. Free energy in the presence of KAM surfaces ($s = 0.8$). (a) Initial points taken along the ($q = 0$) line intersecting the torus seen in Fig. 6(b). The quantity $F^{(14)}$ plotted here practically coincides with $F^{(13)}$. The behavior $F(\beta \geq 1) \equiv 0$ follows from the fact that the interval covering the torus does not shrink with $n$. This form is expected to be the asymptotic result for the free energy obtained with initial conditions corresponding to scattering situations such as, e.g., in (b). (b) The free energy calculated from initial conditions as in Fig. 8. Notice the slow convergence of $F^{(n)}(\beta \geq 1)$, $n = 10, \ldots, 14$, toward the asymptotic $F(\beta) \equiv 0$ value.

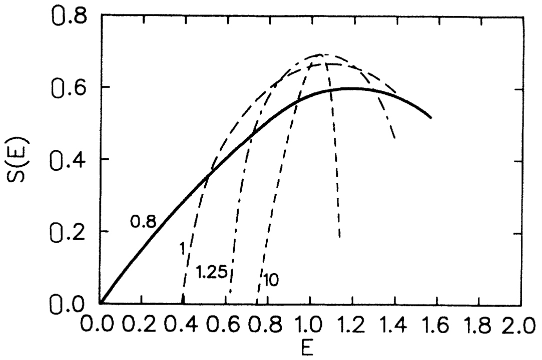

FIG. 10. The Legendre transform $S(E)$ of $\beta F(\beta)$ based on Figs. 8 and 9(a). The support of the entropy function $S(E)$ is the set of all possible local Lyapunov exponents. Its tendency to broaden with decreasing $s$ is in agreement with the bending of the $\beta F(\beta)$ curves seen in Fig. 8. The shortest horizontal distances of these curves to the diagonal give the corresponding escape rates $\kappa$. The graph of the exact $S(E)$ should reach the origin with unit slope in the presence of tori. This reflects the fact that the escape rate is zero and that vanishing local Lyapunov exponents are present in a system where the average Lyapunov exponent $\bar{\lambda}$ is also zero. The right-hand branches of the curves are not complete because of convergence problems of $\beta F(\beta)$ at large negative $\beta$ values.

The topogical entropy starts to decrease first at $s_1$. It is still different from zero at $s_2$ and vanishes only at a much larger field strength $B_c = 1/s_c$. Consequently, in the range $s_c < s < s_2$ the scattering is still irregular and the time delay function exhibits complicated structures. Chaos is, however, no longer present in the sense that the Lyapunov exponent of long trajectories vanishes. The behavior in the range $s_c < s < s_2$ is reminiscent of what is called *strong intermittency* [28] in dissipative systems. Such processes are at the border between regular and chaotic motion. The average Lyapunov exponent is zero, the topological entropy is positive, while the temporal correlations decay in an algebraic fashion, in contrast to

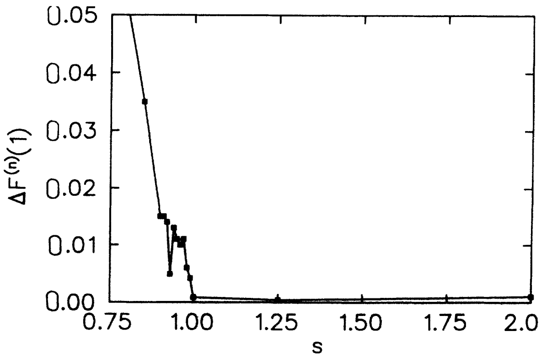

FIG. 11. Fluctuations of the free energy versus cyclotron radius. As a representative example the variance of $F^{(n)}(1)$ computed for the range $n = 10, \ldots, 14$ is plotted. Note the drastic increase around $s_2 = 0.92$ where tori appear, marking a phase-transition-like phenomenon.

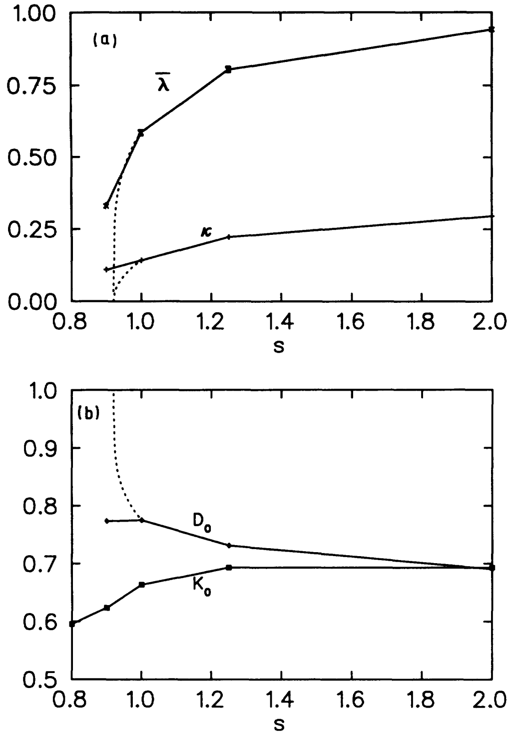

FIG. 12. Dependence of scattering characteristics on the cyclotron radius: (a) $\kappa$ and $\bar{\lambda}$ and (b) $D_0$ and $K_0$. The fact that the measured values of $\kappa$ and $\bar{\lambda}$ for $s = 0.9$ are greater than 0 and that of $D_0$ is less than 1 is due to strong finite size effects. The dashed lines show the expected asymptotic behavior.

the exponential decay characterizing hyperbolic chaotic states. In our system, the borderline behavior is due to the presence of KAM surfaces on the nonattracting invariant set.

## V. DISCUSSION

Based on the example of the three-disk problem, the effect of an external magnetic field on the scattering of charged particles can be summarized as follows. Provided the field-free case is hyperbolic, the system undergoes, with increasing magnetic field at fixed particle energy, four phases characterized by an ever decreasing degree of chaos.

*(i) Hyperbolic phase.* All bounded orbits are strictly hyperbolic and therefore the topological entropy does not change. The magnetic field, however, makes these orbits less unstable. Consequently, the average lifetime of scattering trajectories gradually increases, the escape rate, and the average Lyapunov exponent decreases. Simultaneously, the fractal dimension of scattering singularities increases with the field strength.

*(ii) Pruning-dominated phase.* By a further increase of the field strength certain bounded orbits become stable and thus unaccessible to scattering trajectories. This leads to a decrease of the topological entropy of the nonattracting invariant set underlying the scattering process. The escape rate and the Lyapunov exponent decrease much faster than in the previous phase, but are still different from zero. The fractal dimension exhibits a rapid increase, but does not reach the value of unity yet. In our billiard problem, pruning sets in before KAM tori appear. In cases with smooth potentials these two events are connected and pruning always implies nonhyperbolicity. The size of the tori is, however, first microscopic and one does not realize their presence on time and length scales of the measurement. We thus expect the existence of this phase in smooth potential cases too.

*(iii) Torus-dominated phase.* After KAM tori become of macroscopic size, their stickiness drastically influences the scattering process. The escape rate and the Lyapunov exponent are identically zero independent of the field strength and the fractal dimension of the singularities in the time-delay function becomes unity. Consequently, the scattering is no longer strictly chaotic, although the topological entropy is still nonzero, marking the presence of an infinity of (hyperbolic) orbits in the system. The behavior in this phase is analogous to strong intermittency and is accompanied by diverging fluctuations in the thermodynamic functions. Another drastic difference induced by the appearance of macroscopic tori is the algebraic decay of the correlations characterizing the scattering process in contrast to the exponential behavior in the previous phases.

*(iv) Regular phase.* When the cyclotron radius is sufficiently small, no bouncing is possible among the potential hills. The number of bounded orbits is finite or zero. Consequently, the topological entropy is identically zero and the scattering process is no longer irregular.

The sequence of events described here might provide a general scenario for the transition from chaotic to regular scattering, which occurs when the system is driven away from hyperbolic behavior by the change of some control parameter. In particular, by decreasing the particle energy in the three- or four-hill problem [7,2] (in the absence of an external field) the system goes through the phases described above, although their relative sizes in energy may be very different from those in our example.

It is worth mentioning that the problem of a *closed* billiard in the presence of a magnetic field has recently been studied [29]. Just like in the field-free case [30], opening a small hole in the billiard leads to an escape. Nevertheless, an infinity of bounded orbits survives, which form a nonattractive chaotic set. Our results can thus be of relevance for analyzing subsets of the chaotic domain in closed billiards which are subject to external fields.

Finally, we discuss possible implications of our findings to transport phenomena in semiconductor microjunctions [31,32]. If the size of such mesoscopic junctions is less than the mean free path, transport is ballistic. It has recently been shown [33,31] that many experimental effects can then be reproduced by a model based on the *classical* motion of electrons in *hard-wall billiard* models. The relevance of chaotic scattering in understanding this phenomenon has also been emphasized [34,35]. In semiconductors, at low temperature, a classical ballistic description can typically be valid if the number of reflexions is not greater than about 10 [34], which is of the order of magnitude that can easily be reached numerically. An external magnetic field seems to be the most convenient experimental control parameter.

Even *semiclassical* results have been derived [35,36], which lead to the striking observation that they contain *classical* characteristics of the chaotic scattering process as parameters. In particular, the conductance correlation function averaged over an appropriate wave number interval as a function of the wave number difference is a Lorentzian function. Its half width is proportional to the escape rate, which in hyperbolic cases is inversely proportional to the chaotic lifetime $\tau$ [35]. Other results show that $\tau$ also appears in the frequency-dependent admittance [37].

The junction type used most often is cross shaped, which corresponds to a four-disk problem. This case can be treated along similar lines as the three-hill problem and would lead to the same qualitative results. Thus, based on the magnetic field dependence of the escape rate found in Sec. IV, we predict that, as long as chaotic scattering is relevant, the half width of the conductance correlation function monotonically decreases with increasing magnetic fields. Formally, it tends to zero as soon as the torus-dominated phase is reached, which implies that the correlation function is no longer Lorentzian there. One finds [38] that the correlation function then develops a power-law singularity around the origin, the exponent of which is connected with the exponent characterizing the sticking probablity due to KAM tori.

Another effect of the KAM tori is that long periodic trajectories in their vicinity can accumulate an anomalously large *signed area* [35] and thus *magnetic flux* compared to orbits keeping away from tori. This property causes a power-law decay around the origin in the magnetic field correlation function and leads to an increased high-frequency part in the corresponding power spectrum that is expected to show up in experimental data [39]. These and similar conclusions do not depend on the hard-wall property. The smoothness of the scalar potential might lead, however, to some new details, similarly as in the field-free case [40].

A crossover from chaotic to nonchaotic scattering (from Lorentzian to non-Lorentzian correlation functions) could, in principle, be observed in the stadium billiard used in the experiment of Marcus *et al.* [39] by taking stadia with shorter and shorter straight sides leading finally to a circular billiard. In our paper we have shown that a similar crossover can be studied in another way much easier to realize experimentally by increasing the magnetic flux in the fixed geometry of a three- or four-disk scatterer.

We next add some remarks on the effects associated with deviations of microjunctions from idealized billiards. In a real device the boundary may be rough or inside the scattering domain the potential could be bumpy. These imperfections somewhat deflect the trajectory at each collision from that of a perfect system and lead to deviations from specular scattering. Assuming that the imperfections are distributed randomly, their effect can be considered as a stochastic perturbation of the system. This can be simulated by adding a random angle in the range $(-a\pi, a\pi)$ to $\gamma$ appearing in the Poincaré map [Eqs. (10) and (11)] at each collision with $a$ being the amplitude of the noise (with the obvious restriction that the reflected trajectory of the random system may not penetrate into the disks). Such an investigation has recently been carried out in the case of circular or stadium-shaped microstructures [41] and the qualitative features should also hold in the three-disk geometry. Thus we expect that the first levels of the hierarchical structure of the chaotic invariant set survive a weak disturbance by noise without substantial structural modifications. In the hyperbolic and pruning dominated phases the characteristic numbers would just be shifted by some amounts proportional to $a$. The effect of noise is most drastic in the region corresponding to the deterministic torus-dominated phase. Noise destroys KAM tori: they do not disappear completely, but become perforated so that scattering trajectories can enter the interior of the original tori and leave it as well. This might lead to a weakening of the stickiness effect and, consequently, to a more pronounced hyperbolic behavior.

At last, we give an estimation of the characteristic values of the magnetic field for a system with linear size of the order of magnitude of microjunctions. Since we measure the cyclotron radius in dimensionless units, the relation between the dimensional magnetic field $B$ and $s$ is given by $B = mv/(el_0)s^{-1}$, where $e$, $m$, and $v$ denote the charge, mass, and velocity of the electron, respectively, and $l_0$ is the length unit. As we took the $x$ coordinate of two disks to be unity (see Fig. 1), $l_0$ now yields the dimensional value of this coordinate in microjunction geometries. By choosing $l_0 = 2.5$ $\mu$m and using $v = 10^6$ m/s, which is a realistic value for the Fermi velocity of electrons in semiconductors, we find the following field strengths for the geometry shown in Fig. 1 with aspect ratio $r/d = \sqrt{3}/2$. The value where pruning first sets in is $B_1 = 1.8$ T, while the torus-dominated phase lies between $B_2 = 2.4$ T and $B_c = 9.8$ T. Since $B$ is inversely proportional to $l_0$, a reduction of the linear size by a factor implies the increase of the $B$ values by the same factor.

## ACKNOWLEDGMENTS

The authors are indebted to Professor J. Hajdu and Professor C. Jung for useful discussions and to Professor H. Thomas for carefully reading the manuscript. This work has been partially supported by the Hungarian Scientific Research Foundation under the Grants Nos. OTKA 2090, T4439, F4286, by the Foundation for Hungarian Higher Education and Research, and by the Swiss National Science Foundation. One of the authors (Z. K.) acknowledges the support of the Foundation for Hungarian Science.

## APPENDIX A: THE POINCARÉ MAP

When a particle follows a circular orbit of cyclotron radius $s$, the center of which is situated at $P(p,q)$, and collides with a disk $i$ with center $C(x_i, y_i)$ of radius $r$ at some point $R$ (see Fig. 2), the angle $\gamma$ between the lines $\overline{PC}$ and $\overline{RC}$ is easily obtained from the cosine theorem as

$$\cos\gamma = \frac{w^2 + r^2 - s^2}{2wr}, \tag{A1}$$

where $w$ is the length of the interval $\overline{PC}$ and depends on $p$ and $q$ as $w = [(p - x_i)^2 + (q - y_i)^2]^{1/2}$. Since the image point $P'(p', q')$ is the mirror image of $P$ with respect to the line $\overline{RC}$ corresponding to a rotation of the angle $2\gamma$ around $C$, the explicit form of the map $T$ is obtained as

$$p' = x_i + (p - x_i)\cos 2\gamma - (q - y_i)\sin 2\gamma, \tag{A2}$$

$$q' = y_i + (p - x_i)\sin 2\gamma + (q - y_i)\cos 2\gamma. \tag{A3}$$

It possesses a unit Jacobian as expected for the case of Hamiltonian dynamics.

The Lyapunov numbers of periodic orbits of length $n$ can be computed from the $n$-fold iterated linearized map. Thus they appear as solutions of quadratic equations of the type $\lambda^2 - 2Q\lambda + 1$, where $2Q$ stands for the trace of the $n$-fold iterated linearized map along the cycle. The largest Lyapunov numbers then have the form

$$\lambda = Q + \left(Q^2 - 1\right)^{1/2}. \tag{A4}$$

The Lyapunov number $\lambda_0$ of the bouncing orbit $\overline{01}$ is obtained with

$$Q = Q_0 \equiv \frac{2d}{r} - 1. \tag{A5}$$

Consequently, $\lambda_0$ is independent of $B$. The Lyapunov numbers $\lambda_+$ and $\lambda_-$ of the ring orbits $\bar{1}$ and $\bar{0}$, respectively, are found to have the form of Eq. (A4) with

$$\begin{aligned} Q = Q_\pm &\equiv \cos(2\gamma \pm \pi/3) \\ &\quad + \frac{2d}{\sqrt{3}r}\left(1 \pm \frac{d}{\sqrt{3}p}\right)\left(1 + \frac{s^2 - r^2}{w^2}\right), \end{aligned} \tag{A6}$$

where $\sin\gamma = \sqrt{3}p/(2w)$, $\cos\gamma = \pm[1 - 3p^2/(4w^2)]^{1/2}$,

$$p = \left(s^2 - \left(d - \frac{\sqrt{3}r}{2}\right)^2\right)^{1/2} \mp \left(\frac{d}{\sqrt{3}} - \frac{r}{2}\right) \tag{A7}$$

and

$$w^2 = \left(p \pm \frac{d}{\sqrt{3}}\right)^2 + d^2. \tag{A8}$$

## APPENDIX B: FOUR-SCALE APPROXIMATION TO THE FREE ENERGY

Hyperbolic chaotic sets in the field-free case of the three-disk problem can successfully be described by two-scale approximations. This is a mathematical consequence of the fact that all periodic orbits can be shadowed by two basic ones: they can be glued together from short pieces which are very close to one-half of a bouncing orbit and one-third of a ring orbit rotating between the hills. The Lyapunov exponents of the bouncing orbit and the ring orbit, respectively, are attributed to the corresponding orbit pieces such that the Lyapunov numbers of an arbitrary orbit can approximately be obtained as products of only two basic Lyapunov numbers.

Because of the broken $C_{3v}$ symmetry in the presence of a magnetic field, we have in lowest order three independent Lyapunov numbers determined in Appendix A. It is a natural extension to work out a four-scale approximation expressing the fact that periodic orbits can be built up from four different pieces: from thirds of the clockwise and the counterclockwise period-1 (ring) orbits and from halves of the $\overline{01}$ and the $\overline{10}$ period-2 (bouncing) orbits. The transition probabilities from the symbol 0 to symbols 00 and 01 are proportional to $\lambda_-^{-1}$ and $\lambda_0^{-1}$, respectively. Analogously, the transitions from the symbol 1 to the symbols 10 and 11 are proportional to $\lambda_0^{-1}$ and $\lambda_+^{-1}$, respectively. Assuming asymptotic self-similarity, such processes are characterized [42] by a 2 times 2 matrix,

$$\begin{pmatrix} \lambda_-^{-1} & \lambda_0^{-1} \\ \lambda_0^{-1} & \lambda_+^{-1} \end{pmatrix}. \tag{B1}$$

The escape $\kappa$ rate from the invariant set is obtained from the largest eigenvalue of this matrix, which can be written as $\exp(-\kappa)$.

The entire free energy $F(\beta)$ can also be obtained easily using this approach. To this end, one generalizes the matrix (B1) to a $\beta$-dependent one by replacing in each element the exponents $-1$ by $-\beta$. Then the free energy follows from the largest eigenvalue $\exp[-\beta F(\beta)]$ of this matrix. Thus we obtain

$$\begin{aligned} e^{-\beta F(\beta)} &= \frac{1}{2}\{(\lambda_+^{-\beta} + \lambda_-^{-\beta}) \\ &\quad + [(\lambda_+^{-\beta} - \lambda_-^{-\beta})^2 + 4\lambda_0^{-2\beta}]^{1/2}\}. \end{aligned} \tag{B2}$$

Since hyperbolicity holds for weak magnetic fields, the four-scale approximation is expected to work for large cyclotron radii $s$. In leading order in $1/s$ we obtain

$$\lambda_\pm = \lambda_1\left(1 \pm \frac{A}{s}\right) \tag{B3}$$

with

$$A = \left((2d - \sqrt{3}r)\frac{d}{6}\right)^{1/2}. \tag{B4}$$

The quantity

$$\lambda_1 = \frac{4d}{\sqrt{3}r} - 1 + \left[\left(\frac{2d}{\sqrt{3}r} - 1\right)\frac{8d}{\sqrt{3}r}\right]^{1/2} \tag{B5}$$

is the Lyapunov exponent of the ring periodic orbit without field. By substituting this into the four-scale approximation of the free energy, we obtain in leading order

$$\beta F(\beta) = \beta F_0(\beta) - \frac{A^2}{2}\frac{\beta^2}{s^2}\left(\frac{\lambda_0}{\lambda_1}\right)^{2\beta}\frac{1}{1+(\lambda_0/\lambda_1)^{\beta}}, \quad \text{(B6)}$$

where $F_0(\beta)$ stands for the free energy of the field-free case in the two-scale approximation and

$$\lambda_0 = \frac{2d}{r}\left[1+\left(1-\frac{r}{d}\right)^{1/2}\right] - 1. \quad \text{(B7)}$$

Since the correction term is negative, the graph of $\beta F(\beta)$ vs $\beta$ is less steep for positive $\beta$ than in the field-free case. The decrease of the average Lyapunov exponent $\bar{\lambda}$ and the escape rate $\kappa$ as well as the increase of the fractal dimension $D_0$ follows from this property. Explicit results can be obtained from relations (4)–(7).

---

[1] E. Ott and T. Tél, CHAOS **3**, 417 (1993)

[2] S. Bleher, E. Ott, and C. Grebogi, Phys. Rev. Lett. **63**, 919 (1989); S. Bleher, C. Grebogi, and E. Ott, Physica D 46, 87 (1990).

[3] M. Ding, C. Grebogi, E. Ott, and J. A. Yorke, Phys. Rev. A **42**, 7025 (1990).

[4] U. Smilansky, in *Chaos and Quantum Physics*, edited by M.-J. Giannoni *et al.* (North-Holland, New York, 1992).

[5] T. Tél, in *Directions in Chaos*, edited by Bai-lin Hao (World Scientific, Singapore, 1990), Vol. 3, pp. 149–221.

[6] C. Jung, Acta Phys. Pol. **23**, 177 (1992).

[7] C. Jung and H. J. Scholz, J. Phys. A **20**, 3607 (1987).

[8] B. Eckhardt and C. Jung, J. Phys. A **19**, L829 (1986).

[9] Z. Kovács and T. Tél, Phys. Rev. Lett. **64**, 1617 (1990); T. Tél, Phys. Rev. A **44**, 1034 (1991).

[10] C. Jung and P. Richter, J. Phys. A **23**, 2847 (1990).

[11] T. Tél, J. Phys. A **22**, L691 (1989).

[12] Y. T. Lau, J. M. Finn, and E. Ott, Phys. Rev. Lett. **66**, 978 (1991).

[13] P. Cvitanović, G. Gunaratne, and I. Procaccia, Phys. Rev. A **38**, 1503 (1988).

[14] C. F. Karney, Physica D **8**, 360 (1983); J. D. Meiss and E. Ott, Phys. Rev. Lett. **55**, 2741 (1985); M. Ding, T. Bountis, and E. Ott, Phys. Lett. A **151**, 395 (1990); Y. Lai, C. Grebogi, R. Blümel, and M. Ding, Phys. Rev. A **45**, 8284 (1992); C. F. Hillermeier, R. Blümel, and U. Smilansky, *ibid.* **45**, 3486 (1992).

[15] B. Eckhardt, J. Phys. A **20**, 5971 (1987).

[16] P. Gaspard and S. A. Rice, J. Chem. Phys. **90**, 2225 (1989); **90**, 2242 (1989); **90**, 2255 (1989).

[17] G. Russberg, Ph.D. thesis, NORDITA, Kopenhagen, 1992.

[18] H. E. Nusse and J. Yorke, Physica D **36**, 137 (1989).

[19] D. Ruelle, *Thermodynamic Formalism* (Addison-Wesley, Reading, MA, 1978).

[20] M. J. Feigenbaum, M. H. Jensen, and I. Procaccia, Phys. Rev. Lett. **56**, 1503 (1986).

[21] T. Bohr and D. Rand, Physica D **25**, 387 (1987).

[22] H. Fujisaka, Prog. Theor. Phys. **70**, 1264 (1983); **71**, 513 (1984); P. Grassberger, in *Chaos*, edited by A. Holden (Manchester University Press, Manchester, 1986).

[23] P. Grassberger and I. Procaccia, Phys. Rev. A **28**, 2591 (1983).

[24] P. Grassberger and I. Procaccia, Physica D **13**, 34 (1984).

[25] T. C. Halsey *et al.*, Phys. Rev. A **33**, 1141 (1986).

[26] M. H. Jensen and T. Bohr, Phys. Rev. A **36**, 4904 (1987); T. Yoshida *et al.*, Prog. Theor. Phys. **82**, 879 (1989).

[27] J. Bene, P. Szépfalusy, and A. Fülöp, Phys. Rev. A **40**, 6719 (1989).

[28] S. Grossmann and H. Horner, Z. Phys. B **60**, 79 (1985)

[29] O. Meplan, F. Brut, and C. Gignoux, J. Phys. A **26**, 237 (1993).

[30] O. Legrand and D. Sornette, Europhys. Lett. **11**, 583 (1990).

[31] C. W. J. Beenakker and H. Van Houten, Solid State Phys. **44**, 1 (1991).

[32] H. U. Baranger, D. P. DiVincenzo, R. A. Jalabert, and A. D. Stone, Phys. Rev. B **44**, 10 637 (1991).

[33] C. W. J. Beenakker and H. Van Houten, Phys. Rev. Lett. **63**, 1857 (1989).

[34] M. L. Roukes and O. L. Alerhand, Phys. Rev. Lett. **65**, 1651 (1990).

[35] R. A. Jalabert, H. U. Baranger, and D. Stone, Phys. Rev. Lett. **65**, 2442 (1990); H. U. Baranger, R. A. Jalabert, and D. Stone, Chaos **3**, 665 (1993).

[36] E. Doron, U. Smilansky, and A. Frenkel, Phys. Rev. Lett. **65**, 3072 (1990); Physica D **50**, 367 (1991).

[37] M. Büttiker, A. Pretre, and H. Thomas (unpublished).

[38] Y. Lai, R. Blümel, E. Ott, and C. Grebogi, Phys. Rev. Lett. **68**, 3491 (1992).

[39] C. M. Marcus *et al.*, Phys. Rev. Lett. **69**, 506 (1992); Phys. Rev. B **48**, 2460 (1993); Chaos **3**, 643 (1993).

[40] T. Geisel, R. Ketzmerick, and O. Schedletzky, Phys. Rev. Lett. **69**, 1680 (1992).

[41] W. A. Lin, J. B. Delos, and R. V. Jensen, Chaos **3**, 655 (1993).

[42] M. J. Feigenbaum, J. Stat. Phys. **46**, 919 (1987).

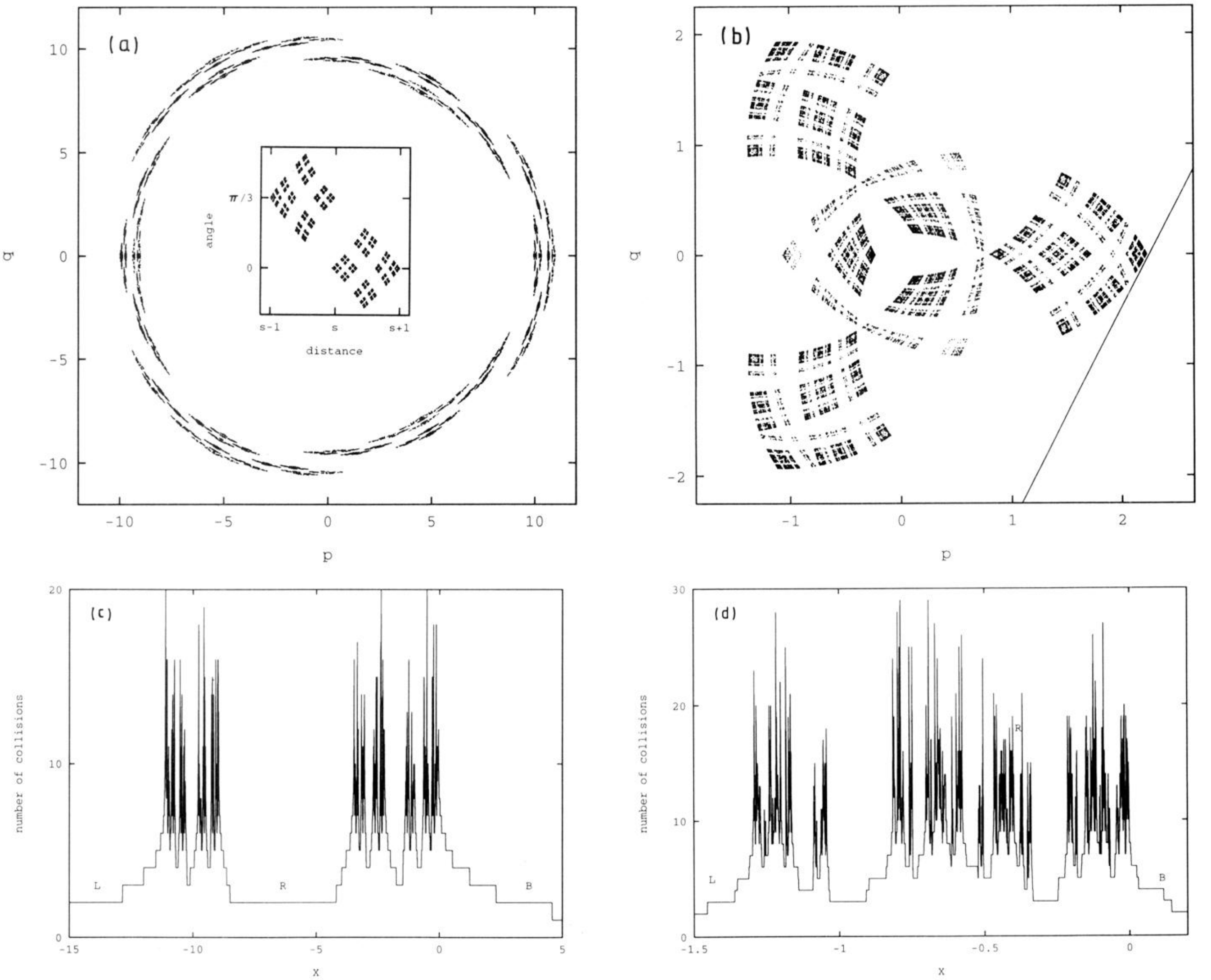

FIG. 4. The chaotic set and the time delay function of the three-disk system for values of the cyclotron radius $s$ when the chaotic set is hyperbolic. (a) The chaotic set for $s = 10$; the inset shows the structure of the rightmost and upper right blocks obtained by an affine transformation. (b) The chaotic set for $s = 1.25$. The straight line, which is parallel to the unstable manifold of the $\overline{01}$ orbit, illustrates the type of initial conditions taken for the time delay functions in this figure and throughout the paper. (c) and (d) display the time delay functions corresponding to (a) and (b), respectively. $X$ is the coordinate along the line of initial conditions measured from the crossing with the $p$ axis ($X > 0$ for $q > 0$). The narrow hole marked by $R$ in (d) corresponds to the first-level large central hole of (c) (see text).

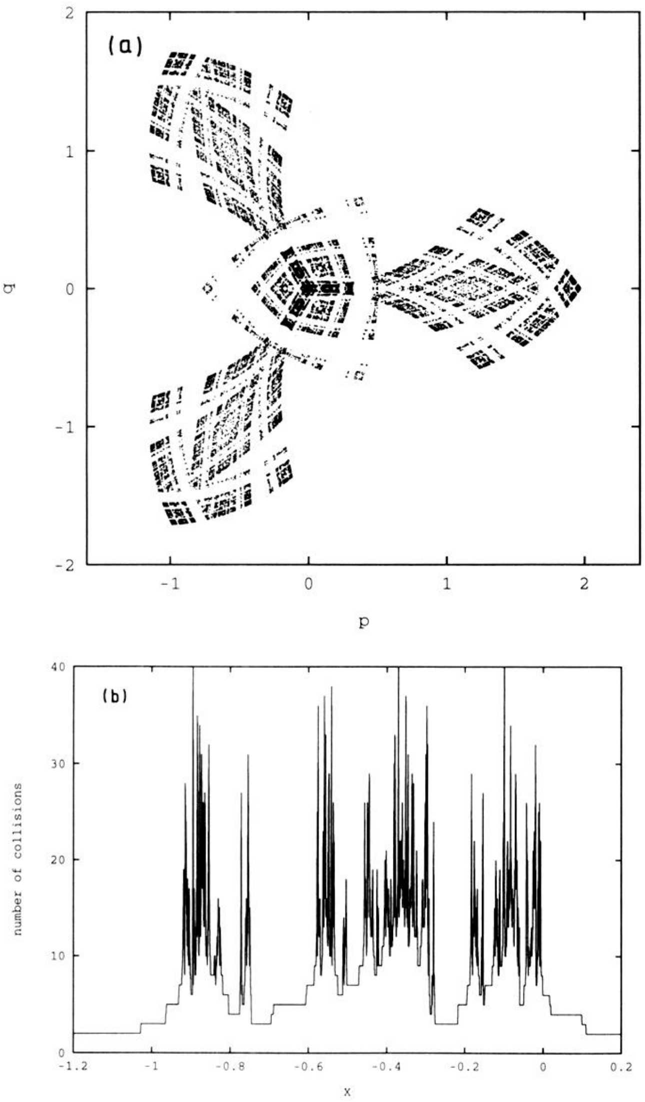

FIG. 5. (a) The chaotic set for $s = 1.0$ when pruning has set in. Some corners of the blocks have collided and disappeared. (b) The corresponding time delay function. The first level hole $R$ of Fig. 4(d) is missing here.

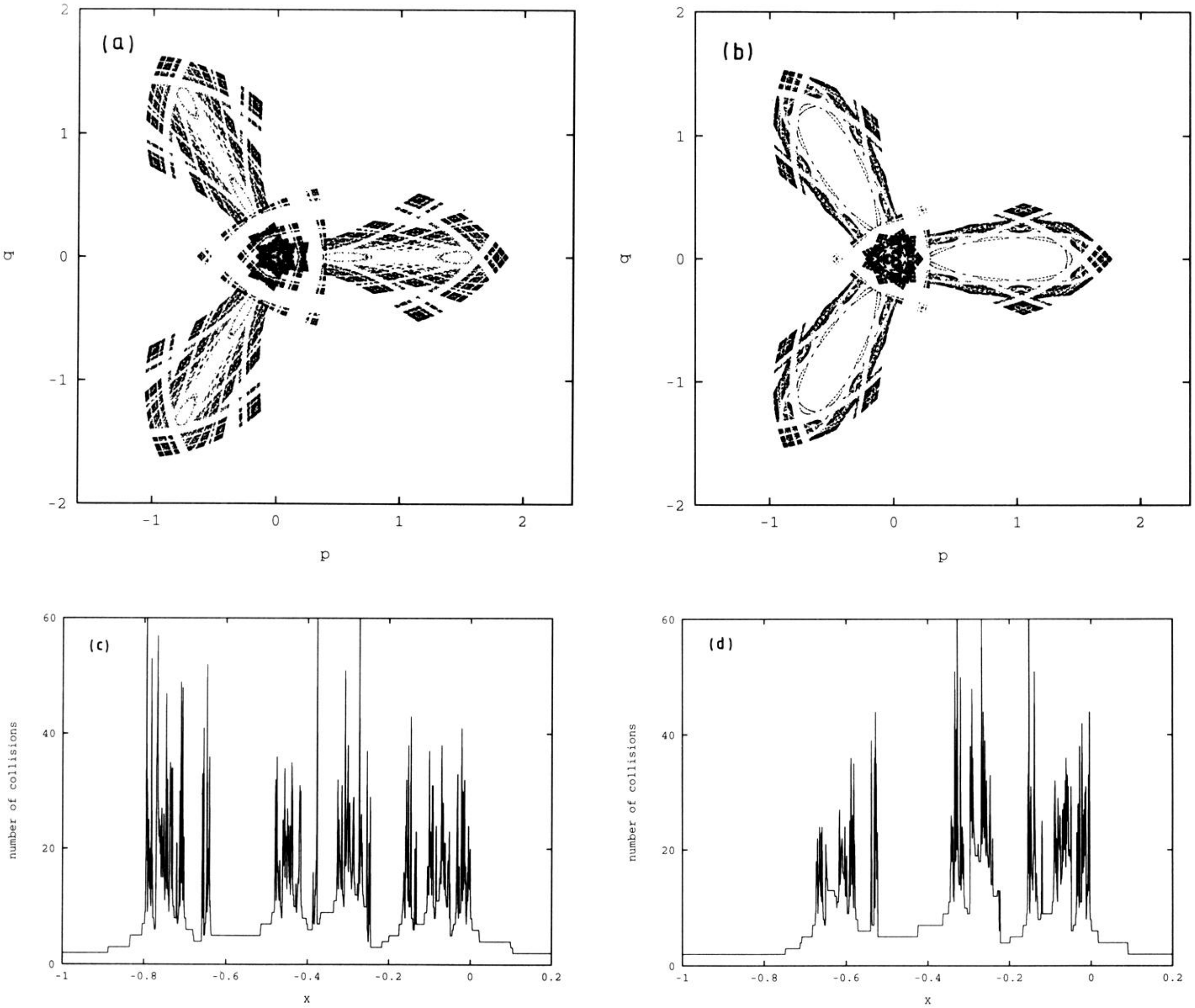

FIG. 6. The chaotic set for $s = 0.9$ (a) and 0.8 (b) with stable islands and the corresponding time delay plots [(c) and (d), respectively].